The effects of oxide evolution on mechanical properties in proton- and neutron-irradiated Fe-9%Cr ODS steel

M.J. Swenson [a, *], C.K. Dolph [a], J.P. Wharry [a, b]

[a] Boise State University, 1910 University Drive, Boise, ID 83725, USA
[b] Purdue University, 400 Central Drive, West Lafayette, IN 47907, USA

ABSTRACT

The objective of this study is to evaluate the effect of irradiation on the strengthening mechanisms of a model Fe-9%Cr oxide dispersion strengthened steel. The alloy was irradiated with protons or neutrons to a dose of 3 displacements per atoms at 500 °C. Nanoindentation was used to measure strengthening due to irradiation, with neutron irradiation causing a greater increase in yield strength than proton irradiation. The irradiated microstructures were characterized using transmission electron microscopy and atom probe tomography (APT). Cluster analysis reveals solute migration from the Y-Ti-O-rich nanoclusters to the surrounding matrix after both irradiations, though the effect is more pronounced in the neutron-irradiated specimen. Because the dissolved oxygen atoms occupy interstitial sites in the iron matrix, they contribute significantly to solid solution strengthening. The dispersed barrier hardening model relates microstructure evolution to the change in yield strength, but is only accurate if solid solution contributions to strengthening are considered simultaneously.

© 2016 Elsevier B.V. All rights reserved.

1. Introduction & background

The growing global demand for energy will increasingly call upon fusion and advanced nuclear fission reactors to supply safe and reliable energy worldwide. These reactor designs require structural and cladding materials that can withstand temperatures up to 700 °C, and irradiation doses up to several hundred displacements per atom (dpa) [1–3]. Oxide dispersion strengthened (ODS) steels are candidates for advanced reactor cladding materials and fusion first wall and blanket structures, due to their high-temperature strength and dimensional stability under irradiation [4–13]. A key microstructural feature of ODS steels is their high density of Ti-Y-O-rich nanoclusters, which act as localized sinks for point defects, providing resistance to irradiation swelling [4–6,8–10,12]. These clusters also strengthen the material without significantly compromising ductility.

Before ODS steels can be utilized in nuclear power plants, however, their long-term strength and mechanical integrity, especially under irradiation, must be understood. It is well known that irradiation-induced microstructural features such as voids and

dislocation loops increase the strength of a material by acting as obstacles to impede dislocation motion during deformation. Likewise, the oxide nanoclusters also serve as dislocation pinning points, but their irradiation stability is governed by two competing mechanisms: (1) ballistic dissolution due to irradiation damage cascades, and (2) enhanced diffusion driving solute atoms to recombine (i.e. ripening) [14–16]. As a result, it is necessary to understand the relationship between microstructure evolution and macroscopic material properties of ODS under irradiation.

The simplified dispersed barrier hardening model is most commonly used for relating microstructure to macroscopic mechanical properties such as yield stress. In applying this model, the fundamental challenge lies in estimating the relative barrier strength, α_i, for each obstacle type i. Over the years, studies have provided guidelines to directly estimate α_i [17,18]. But it is expected that α_i values are influenced by many sample-specific characteristics such as nanocluster composition and coherency, void faceting, and dislocation loop habit planes [19]. As a result, the values for each α_i will likely vary from sample to sample. To attain sample-specific α_i values, some studies have calculated the relative obstacle strengths necessary to mathematically relate the microstructure to the measured mechanical behavior (via indentation or tensile testing techniques) [19–21]. Adding to the complexity, additional studies have suggested that the strength of each obstacle

---

is also dependent upon the size and/or number density of the obstacles in the matrix of the material [10,22–24]. All of these approaches have provided valuable insight into how dislocations interact with different types of obstacles. However, very few irradiation experiments have considered the evolution of solid solution strengthening as a significant contributor.

The objective of this study is to evaluate the effects of irradiation on the strengthening mechanisms of an ODS steel. This objective is achieved by developing an analytical model that combines dispersed barrier hardening with solid solution strengthening to more accurately relate the microstructure of an irradiated ODS steel to its mechanical hardness. The influence of solute migration from the oxides to the matrix (via dissolution) is closely considered. Different methods for estimating the strength factors for the dispersed barriers are compared and multiple approaches for superimposing the effects of each type of dispersed barrier are applied. Finally, an evaluation of the potential coherency of the oxide nanoclusters and its relationship to the size of the clusters is discussed.

2. Experiments

2.1. Material, irradiations, and microscopy

A rod of Fe-9%Cr ODS martensitic steel material (composition provided in Table 1) was provided by the Japan Nuclear Cycle Development Institute (now known as the Japan Atomic Energy Agency). The rod was processed by mechanically alloying ferritic steel with Y_2O_3 powders, then hot extruding at 1150 °C. Finally, the rod was heat treated at 1050 °C for 1 h, air cooled, then tempered at 800 °C with subsequent air cooling. Additional details regarding the mechanical alloying and fabrication of the rod may be found in Ref. [25]. Two sets of specimens were cut from the rod: one set for proton irradiations, and another set for neutron irradiation. Both irradiations are carried out to 3 dpa at 500 °C. For proton-irradiation, the displacement damage of 3 dpa and the damage depth profile had been calculated with the Stopping and Range of Ions in Matter (SRIM-2008) program [26]. A flux of 2.0 MeV protons normal to Fe-9%Cr produces a relatively uniform damage profile between 1 μm and 10 μm, with a damage peak at approximately 19 μm (shown in Fig. 1). All details for sample preparation, proton irradiation and neutron irradiation may be found in Ref. [27].

TEM analysis was conducted to evaluate microstructure evolution under proton or neutron irradiation. TEM lamellae were prepared from the as-received and irradiated conditions using the same focused ion beam (FIB) lift-out technique on an FEI Quanta 3D FEG FIB at the Center for Advanced Energy Studies (CAES). All details regarding the TEM sample preparation and analysis may be found in Ref. [27].

Atom probe tomography (APT) complemented the TEM analysis by enabling atomic-resolution characterization of the oxide nanoclusters and nanoscale phases. APT needles were fabricated by FIB milling from the as-received, proton-irradiated, and neutron-irradiated specimens at CAES. Cluster analysis was performed on each tip (excluding those volumes attributed to carbides or grain boundaries) using the maximum separation method [28] with the cluster analysis module within the IVAS software. All details
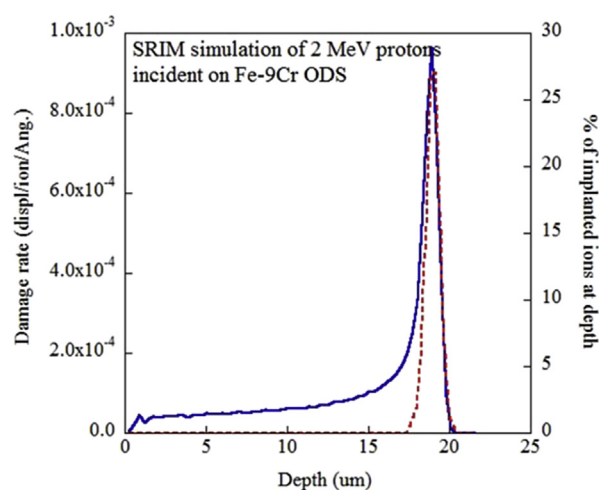

Fig. 1. SRIM-2008 [26] calculation of damage profile for 2 MeV proton irradiation normal to Fe-9Cr in "Detailed Calculation" mode.

regarding the atom probe tomography sample preparation and analysis may be found in Ref. [27].

2.2. Nanoindentation

Nanoindentation was conducted to assess the hardness of the irradiated samples relative to the as-received material. To minimize the effects of sample-to-sample surface finish variations, the as-received specimen was prepared in the same manner as the irradiated specimens: mechanically polished through 4000 grit SiC paper, followed by electropolishing. Indentations were made with a vibration isolated Hysitron TI-950 TriboIndenter at CAES using a high load transducer and a Berkovich indenter with 250 nm tip radius. For the irradiated specimens, indents were made in top-down orientation onto the irradiated surface (oriented parallel to the irradiating beam). Indents were executed in depth-controlled mode ranging from 100 nm to 1000 nm, in 100 nm increments, to determine nanohardness as a function of depth. The plastic zone of each indent is expected to be 5–10 times deeper than the indent itself [29–34], which corresponds to the flat region of the damage profile where dose is calculated, and avoids the damage peak (see Fig. 1). Indents were placed a minimum of 60 μm apart to prevent overlap and interaction of the plastic zones of neighboring indents. A contact threshold of 250 μN was used with a three segment loading curve (20 s loading period, five second hold period, and a 20 s unloading period) that was verified to reduce creep effects within the system during testing. A minimum of 13 indents were performed at each depth to ensure 95% confidence that the measured nano-hardness values are within a 5% margin of error. Size limitations of the neutron-irradiated sample provided limited statistics at the 600 nm and 900 nm depths, leading to a 90% confidence for those indentation depths. Analysis of the indentation data was conducted using the Oliver-Pharr method with the TriboScan MP 9.3.13.0 software, and any statistical outliers were

Table 1
Chemical composition of Fe-9%Cr ODS.

Chemical composition (wt%, balance Fe)														
C	Si	Mn	P	S	Ni	Cr	W	Ti	Y	O	N	Ar	Y_2O_3	Ex. O
0.14	0.048	0.05	<0.005	0.004	0.06	8.67	1.96	0.23	0.27	0.14	0.017	0.004	0.34	0.07

$[Y_2O_3] = 1.27 \times [Y]$
$[Ex.O] = [Total O]–[O \text{ in } Y_2O_3 \text{ powder}] = [O]–0.27 \times [Y]$

removed. Nanoindentation of the as-received specimen was also conducted in the aforementioned manner.

3. Results

3.1. Transmission electron microscopy

TEM imaging was used to observe the microstructure of irradiated and as-received specimens. Quantitative TEM microstructure results are provided in Table 2 for all specimen conditions.

Approximately 100 grains and the carbide precipitates contained within them were measured from each condition. Grains and carbides exhibit little change with irradiation, having diameters ranging 0.23–0.31 μm and 0.07–0.11 μm, respectively. All diameter variations fall within the standard deviation of the measurements. Similarly, the dislocation line density varies over 17.6–19.1 $\times$ 10^{14} m^{-2} with a standard deviation up to 5.3 $\times$ 10^{14} m^{-2}. Based on these relatively narrow bands of size and density measurements, and their corresponding wide standard deviations, there is no evidence to suggest that these features have dramatically evolved in response to either irradiation condition.

Small irradiation-induced voids, 3–7 nm in diameter, are observed at a low number density of 0.24–0.34 $\times$ 10^{21} m^{-3} in both the proton- and neutron-irradiated specimens. TEM micrographs of typical voids may be found in Ref. [27] for the proton- and neutron-irradiated conditions, respectively.

Dislocation loops were imaged in STEM mode at the [001] and [111] zone axes. For each zone axis imaged, dislocation loop orientation maps generated by Yao et al. [35] were used to determine that the loops commonly resided on the {111} or {001} habit planes [35]. Dislocation loops produced by proton and neutron irradiation are similar in size, at 8.4 and 8.9 nm, respectively, and similar in number density, at 10.2 $\pm$ 8.0 $\times$ 10^{21} m^{-3} and 2.3 $\pm$ 1.2 $\times$ 10^{21} m^{-3}, respectively. STEM micrographs of typical distributions of dislocation loops may be found in Ref. [27].

Bright field images of the oxide clusters were obtained by reviewing areas that had low dislocation contrast, which allowed the z-contrast of the clusters to be more visibly prominent. With this technique, it becomes difficult to resolve any nanoclusters that are less than ~2 nm in diameter [6,36]. As a result, atom probe tomography was also conducted to achieve a more objective determination of the oxide nanocluster average size, number density and composition. Additional details regarding the TEM analysis may be found in Ref. [27].

3.2. Atom probe tomography

The atomic-level resolution of APT with IVAS cluster analysis enabled the characterization of the oxide nanoclusters prior to and after irradiation. The 3D reconstructions of the as-received specimens exhibit clustering of Ti, O and Y atoms along with TiO, YO, FeO, and CrO compounds all at coincident locations in the matrix. For this reason, all of these atoms/compounds were chosen for the oxide cluster analysis in each condition. Representative atom distribution maps Ti, O, and Y atoms, and TiO and YO compounds, as well as the 3D cluster reconstruction, are found in Ref. [27] for the as-received, proton-irradiated, and neutron-irradiated conditions.

Cluster analysis using IVAS software enables quantification of the oxide nanocluster sizes and number densities (Table 3). A total of 486, 964, and 355 oxide nanoclusters were identified and analyzed in the as-received, proton–irradiated, and neutron-irradiated specimens, respectively. Proton irradiation caused the average size of the nanoclusters to decrease from 5.96 $\pm$ 3.10 nm to 4.77 $\pm$ 1.91 nm, at a similar number density (568 $\times$ 10^{21} m^{-3} as-received, to 560 $\times$ 10^{21} m^{-3} proton-irradiated). However, neutron irradiation induced a more significant decrease in nanocluster size and number density, to 3.41 $\pm$ 1.69 nm at 435 $\times$ 10^{21} m^{-3}. Both the decline in average size and number density of the nanoclusters are reflected in the reduced volume fraction and suggest partial dissolution of the nanoclusters into the matrix. This result is described in greater detail in Ref. [27]. Ref. [27] describes this result in greater detail and summarizes existing archival literature studies in which irradiation-induced oxide nanocluster coarsening, dissolution, and stability have all been observed depending upon the target alloy and irradiation conditions.

The enrichment parameter f_{en}^i, represents the percent of all collected ions of species i, above the bulk volume fraction, which is contained in the analyzed clusters. This is a key parameter from APT

Table 2
Summary of microstructural measurements using TEM, from Ref. [27].

Feature	Measurement	As-received	Proton-irradiated (3 dpa, 500 °C)	Neutron-irradiated (3 dpa, 500 °C)
Grains/Laths	# of grains measured	104	104	104
	Effective diameter ($\times 10^{-6}$ m)	0.23 $\pm$ 0.12	0.31 $\pm$ 0.11	0.31 $\pm$ 0.09
Dislocation lines	# of measurements	17	46	39
	Density ($\times 10^{14}$ m^{-2})	19.1 $\pm$ 3.8	17.6 $\pm$ 5.3	18.5 $\pm$ 4.8
Carbide precipitates	# of carbides measured	36	51	68
	Effective diameter ($\times 10^{-6}$ m)	0.11 $\pm$ 0.07	0.07 $\pm$ 0.03	0.10 $\pm$ 0.06
	Density ($\times 10^{20}$ m^{-3})	0.20	0.46	0.47
Voids	# of voids measured	0	8	22
	Diameter ($\times 10^{-9}$ m)	–	4.00 $\pm$ 1.51	3.64 $\pm$ 1.14
	Density ($\times 10^{21}$ m^{-3})	–	0.34 $\pm$ 0.44	0.24 $\pm$ 0.12
Dislocation loops	# of loops measured	0	688	182
	Diameter ($\times 10^{-9}$ m)	–	8.4 $\pm$ 1.7	8.9 $\pm$ 2.0
	Density ($\times 10^{21}$ m^{-3})	–	10.2 $\pm$ 8.0	2.7 $\pm$ 0.7

Table 3
Summary of oxide nanocluster and matrix composition measurements for as-received, proton-irradiated and neutron-irradiated conditions using APT, from Ref. [27].

Oxide nanoclusters	As-received	Proton-irradiated (3 dpa, 500 °C)	Neutron-irradiated (3 dpa, 500 °C)
# of clusters measured, ΣN_c	486	964	335
Analysis Volume, V_T (nm^3)	856,053	1,722,204	816,586
Average Diameter, D_G (nm)	5.96	4.77	3.41
Standard deviation for D_G	$\pm$3.10	$\pm$1.91	$\pm$1.69
Std. dev. of the mean for D_G	$\pm$0.14	$\pm$0.06	$\pm$0.09
Density, N_{nc} ($\times 10^{21}$ m^{-3})	568	560	435
Volume fraction, f_v	5.2%	5.1%	2.4%
Species enrichment, f_{en}^i (above volume fraction)			
Y	68.9%	76.2%	49.7%
Ti	66.2%	60.4%	21.6%
O	61.1%	62.6%	29.9%
Cr[a]	1.0%	2.2%	0.9%
Si	2.0%	6.0%	5.9%
Mn	0.7%	1.7%	3.6%
Ni	2.9%	11.7%	5.9%
C[a]	5.4%	8.4%	2.0%
W[a]	−0.1%	−1.9%	−0.6%
Matrix composition, C_i (at%)			
Y	0.05%	0.04%	0.10%
Ti	0.11%	0.15%	0.32%
O	0.17%	0.19%	0.37%
Cr	8.38%	8.21%	8.14%
Si	0.15%	0.13%	0.12%
Mn	0.06%	0.06%	0.08%
Ni	0.03%	0.03%	0.05%
C	0.15%	0.12%	0.16%
W	0.61%	0.60%	0.67%

Trace amounts of P, S, N and H, Ga detected (balance is Fe).
[a] Does not include species clustering in carbide precipitates.

cluster analysis that enables comparison of nanocluster chemistry from sample to sample. The f_{en}^i of Y, Ti, and O remain relatively unchanged with proton irradiation (Table 3), suggesting that little de-clustering of the oxides occurs with proton irradiation. Meanwhile, there is a notable decrease in f_{en}^Y, f_{en}^{Ti}, and f_{en}^O following neutron irradiation. One of the most pivotal de-clustering species is measured for O; prior to irradiation, 61.1% of all O ions above the base volume fraction are clustered, compared to only 29.9% enrichment following neutron irradiation. As expected, the matrix composition generally demonstrates an opposite trend (Table 3). For elements that exhibit reduced enrichment in clusters upon irradiation (Y, Ti, and O) there is a corresponding increase in matrix concentration. For elements that exhibit increased enrichment upon irradiation (Si, Mn, and Ni), there is a corresponding decrease in matrix concentration.

3.3. Nanoindentation

Top-down nanoindentation results show the nanohardness of the as-received and irradiated specimens as a function of depth, Fig. 2. At lower depths (<400 nm) there is evidence of the effect of surface roughness on nanohardness measurements for each of the samples. In particular, the proton-irradiated surface was not subsequently polished following irradiation, so a greater surface roughness is expected due to surface sputtering during irradiation. As a result, the nanohardness of each specimen was calculated by taking an average of the measured values from depths ≥500 nm and the standard deviation of the mean for each. The nanohardness is estimated to be 4.58 ± 0.20 GPa, 4.60 ± 0.11 GPa and 4.97 ± 0.07 GPa for the as-received, proton-irradiated and neutron-irradiated, respectively. Although the relative error at each data point may seem large, it is clear the neutron-irradiated specimen is harder than both the as-received and proton-irradiated specimens, outside of the error bars. The measured hardness values for the as-received specimen compare well to nanohardness values of 4.49−4.63 GPa measured by Liu et al. [12] on as-received F82H ODS, and 3.8 GPa measured by Huang et al. [34] on as-received PM2000 ODS. Additionally, Hosemann, et al. [37] measured hardness values of 5−5.25 GPa on Fe-8Cr-2W ODS after neutron irradiation to 20.3 dpa at 400 °C.
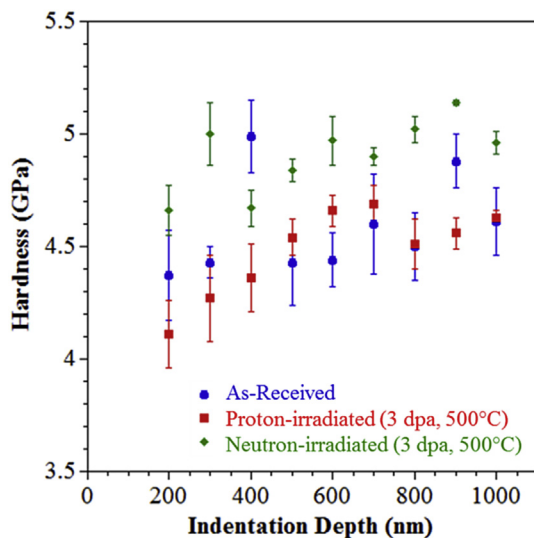

Fig. 2. Nanoindentation hardness of Fe-9%Cr ODS for as-received and after proton irradiation or neutron irradiation to 3 dpa at 500 °C, indented parallel to irradiation beam at various indentation depths.

Nanohardness measurements can be used to estimate the increase in yield strength as a result of irradiation, through the empirical relationship [38]:

$$\Delta\sigma_y = 3.06\Delta H_v \tag{1}$$

with $\Delta\sigma_y$ as the increase in yield strength (in MPa) and ΔH_v as the measured increase in hardness (in kg/mm^2). Although Eq. (1) was developed for Vickers microhardness measurements, Hosemann, et al. [37] have shown that nanohardness and microhardness measurements have produced consistent results on an Fe-8Cr-2W ODS alloy. Fischer-Cripps has also identified that Berkovich hardness (in GPa) may be converted to Vickers hardness (in kg/mm^2) by the relationship $H_V = 94.495 H_{Berk}$ [39]. This conversion, along with Eq. (1), estimates the change in yield strength of the Fe-9%Cr ODS studied herein to be 6 MPa and 112 MPa upon proton and neutron irradiation, respectively. These results are consistent with measurements in the archival literature. For example, McClintock, et al. [40] irradiated 14YWT with neutrons to 1.5 dpa at 580 °C and 300 °C, then measured 33 MPa and 125 MPa strengthening, respectively. Meanwhile, Ramar, et al. [41] measured 44 MPa strengthening in ODS Eurofer 97 after proton irradiation to 2 dpa at 40 °C. So overall, ODS alloys tend not to exhibit dramatic strengthening, at all irradiation temperatures.

4. Discussion

4.1. Dispersed barrier hardening

Defects such as voids, dislocation loops, and nanoclusters within the matrix of a material are barriers to dislocation motion, and thus contribute to the overall strength of a material. Since the morphology of these features is often influenced by irradiation, changes to the hardness and strength of the material often result. The most common method for relating discrete microstructural features to the yield strength is the simplified dispersed barrier hardening model [42], written as:

$$\Delta\sigma_{y,i} = \alpha_i M\mu b\sqrt{N_i d_i} \tag{2}$$

In this equation, M is the Taylor factor (3.06 for b.c.c. Fe-Cr alloys such as the ODS of interest [18]), μ is the shear modulus (82 GPa for ODS [43]), b is the Burger's vector (0.248 nm [43]), N_i is the number density of feature type i, and d_i is the average diameter of feature i. The factor α_i represents the barrier strength of feature i and should be a coefficient valued between 0 and 1. A feature with a low α is considered a weak obstacle that more readily allows dislocations to bypass or shear through them, while features with α approaching a value of 1 are considered to be stronger inhibitors to dislocation motion. Equation (2) may be written for each type of feature present, then superimposed upon each other to calculate an overall net increase in yield strength from a network of microstructural features [18,44,45].

For the ODS alloy studied here, Eq. (2) is used to predict strengthening due to the evolution of oxide nanoclusters, voids, and dislocation loops upon proton or neutron irradiation. The term $\sqrt{N_i d_i}$ for voids, dislocation loops, and oxide nanoclusters (as seen from Tables 2 and 3) will be higher for the proton irradiated sample than for the neutron irradiated sample. It then follows that the Eq. (2) predicted strengthening of the proton irradiated specimen would be higher than that of the neutron irradiated specimen. However, this is contrary to the nanoindentation results (Fig. 2), which indicate that very little (if any) proton irradiation hardening occurs, while neutron irradiation causes a ~112 MPa increase in yield strength. As a result of these seemingly contradictory findings,

it is hypothesized that additional strengthening mechanisms work along with dispersed barrier hardening to produce the increased strengthening in ODS upon neutron irradiation.

In the following sections, solid solution strengthening will be considered as an additional strengthening mechanism, and it will be combined with the dispersed barrier hardening model. Alternative methodologies for estimating the barrier strengths (α_i) for each type of microstructural feature will also be reviewed, along with different approaches to superimpose the individual strengthening contributions of each feature type.

4.2. Solid solution strengthening

A model is implemented for the solid solution strengthening contribution of each solute species. The cluster analysis module in the IVAS software enables accurate quantification of the number of atoms of each elemental specie within every cluster and within the matrix. From this data, the elemental composition of the surrounding matrix may be calculated and utilized in the solid solution strengthening model for a b.c.c. Fe matrix [46,47]:

$$\Delta\sigma_{ss,i} = K_i C_i \tag{3}$$

in which $\Delta\sigma_{ss,i}$ is the resultant change in yield strength due to solid solution strengthening, K_i is the strengthening coefficient of the solute element, and C_i is the composition of the solutes in the matrix. Equation (3) may be applied for each solute element, then the overall solid solution strengthening effect may be calculated using [46]:

$$\Delta\sigma_{ss} = \sum_i \Delta\sigma_{ss,i} \tag{4}$$

Estimated values of K_i from prior studies are tabulated in Table 4 from Refs. [46–49] for solutes in b.c.c. Fe. One particular observation is that interstitial solute species such as C and N have a strengthening factor K that is 2–3 orders of magnitude greater (~1000 MPa/at%) than K factors for solutes that occupy substitutional positions [47]. Since O is also believed to take interstitial sites in b.c.c. Fe [48], it would be expected that K_O would have a similar order of magnitude as K_C and K_N. Limited data is available for the K factors of W and Y in b.c.c. Fe. But since these elements are predominantly substitutional solutes, their strengthening coefficient is estimated to be similar to that of other substitutional elements (~20 MPa/at%).

Using the estimated strengthening coefficients from Table 4 and the measured matrix composition from Table 3, the calculated solid solution strengthening effects from Eqs. (3) and (4) are presented in Table 5. Although there are minor compositional changes in the matrix for substitutional atoms such as Si, Mn, Ni, Cr, W, Ti, and Y, these changes have an essentially negligible effect on the overall strengthening of the alloy. For this reason, most irradiation experiments will generally ignore solid solution strengthening as a source of irradiation-induced hardening. However, for ODS alloys, the primary species contained in the oxide nanoclusters are Ti, Y, and O. Because O is an interstitial solute, any O atoms that diffuse out of the oxide nanoclusters and into the matrix, or vice versa, will have a significant impact on the solid solution strengthening. From Table 5, the estimated strengthening effect of matrix O is 171 MPa in the as-received condition and increases to 187 MPa and 370 MPa after proton and neutron irradiation, respectively. This result corresponds to the increase in matrix O content attributed to irradiation-induced oxide dissolution. Overall, the combined strengthening of all matrix solutes considered is 368 MPa in the as-

received condition, 348 MPa following proton irradiation representing a net solid solution softening of 20 MPa, and 581 MPa after neutron irradiation representing a net solid solution strengthening of 213 MPa.

These calculated changes in solid solution strengthening are consistent with the generally unchanged yield strength with proton irradiation, and the yield strength increase with neutron irradiation. In the next section, this solid solution strengthening will be combined with the dispersed barrier hardening model to develop a more robust correlation between the microstructure and yield stress.

4.3. Combining dispersed barrier and solid solution hardening

There are two fundamental challenges to combining the simplified dispersed barrier hardening model (Eq. (2)) with solid solution strengthening. First is the challenge of determining appropriate barrier strengths, α_i, for each feature (for the dispersed barrier hardening contributions). Second is to establish an accurate method to superimpose the strengthening contribution of multiple types of barriers impeding dislocation motion (nanoclusters, voids, dislocation loops, solutes, etc.). A further complication is that these challenges are interdependent and there are more α_i variables (i.e. unknowns) than there are equations, so the system cannot be solved algebraically. Rather, the system can only be solved if some variable(s) are assumed. In this section, we present three different approaches for estimating the α_i values. Within each of these three approaches, we consider two methods for superimposing the effects of multiple barriers: linear superposition and root-sum-square superposition. In total, then, there are six sets of solutions for α_i and superimposed strengthening. Comparison of these solution sets with measured nanohardness reveals insights into the strengthening mechanisms active in irradiated ODS.

First we establish expressions for the linear and root-sum-square superposition methods. Linear superposition is generically written as [18]:

$$\Delta\sigma_{y,l} = \sum_i \Delta\sigma_{y,i} \tag{5}$$

and is considered more applicable when the obstacles have widely differing strengths. To determine the irradiation-induced change in yield strength, the linear superposition of the as-received microstructure is subtracted from the linear superposition of the irradiated microstructure. For the ODS alloy studied here, only oxide nanoclusters, dislocation loops, voids, and the solid solution are considered; dislocation lines, carbides, and grain boundaries are not considered because they exhibit no statistical change under irradiation. The **linear superposition** expression for irradiation-induced strengthening is then:

$$\Delta\sigma_{y,l} = \Delta\sigma_{nc}^{irr} + \Delta\sigma_{v}^{irr} + \Delta\sigma_{l}^{irr} - \Delta\sigma_{nc}^{ar} + \Delta\sigma_{ss}^{irr} - \Delta\sigma_{ss}^{ar} \tag{6}$$

where subscripts nc, v, l, and ss represent nanoclusters, voids, loops, and solid solution, respectively, and superscripts irr and ar represent the irradiated and as-received material, respectively.

Root-sum-square superposition is written as [18]:

$$\Delta\sigma_{y,r} = \sqrt{\sum_i \left(\Delta\sigma_{y,i}\right)^2} \tag{7}$$

and is considered more accurate when the obstacles have similar strengths. The **root-sum-square superposition** expression for irradiation-induced strengthening is then:

Table 4
Solid solution strengthening coefficients for solute elements at room temperature (in MPa/at%), from Refs. [46–49].

Element	Substitutional or interstitial	Ref. [48]	Ref. [47]	Ref. [49]	Ref. [46]	Value used in this study
C	Interstitial	–	~1050	–	1103.45	1000
N	Interstitial	–	~1050	–	1103.45	–
O	Interstitial	–	–	–	–	1000[a]
Si	Substitutional	49–55	45	–	25.8	30
Mn	Substitutional	35–40	33	–	16.9	20
Ni	Substitutional	35–41	2.9	–	19.2	20
Cr	Substitutional	5–9	–	2.5–3.5	2.6	3
W	Substitutional	–	–	–	–	20[a]
Ti	Substitutional	–	–	–	17.9	20
Y	Substitutional	–	–	–	–	20[a]

[a] Estimated based on status as substitutional or interstitial solute type.

Table 5
Matrix composition and calculated solid solution strengthening effects using Eqs. (3) and (4).

Element	As-received		Proton-irradiated (3 dpa, 500 °C)		Neutron-irradiated (3 dpa, 500 °C)	
	C_i (at%)	$\Delta\sigma_{ss,i}$ (MPa)	C_i (at%)	$\Delta\sigma_{ss,i}$ (MPa)	C_i (at%)	$\Delta\sigma_{ss,i}$ (MPa)
C	0.15	150	0.12	115	0.16	159
Si	0.15	5	0.13	4	0.12	4
Mn	0.06	1	0.06	1	0.08	2
Ni	0.03	1	0.03	1	0.05	1
Cr	8.38	25	8.21	25	8.14	24
W	0.61	12	0.60	12	0.67	13
Ti	0.11	2	0.15	3	0.32	6
Y	0.05	1	0.04	1	0.10	2
O	0.17	171	0.19	187	0.37	370
Total solid solution strengthening (MPa)	368		348		581	
Solid solution strengthening (MPa) − above as-received	–		−20		213	

$$\Delta\sigma_{y,r}^{irr} = \sqrt{\Delta\sigma_{nc}^{irr2} + \Delta\sigma_{v}^{irr2} + \Delta\sigma_{l}^{irr2}} - \Delta\sigma_{nc}^{ar} + \Delta\sigma_{ss}^{irr} - \Delta\sigma_{ss}^{ar} \qquad (8)$$

It should also be noted that a mixed approach, introduced by Odette and Lucas [44], uses a weighting parameter S based on the relative strengths of the strongest and weakest barriers as:

$$\Delta\sigma_y = S\left(\Delta\sigma_{y,l} - \Delta\sigma_{y,r}\right) + \Delta\sigma_{y,r} \qquad (9)$$

$$S = \alpha_s - 5\alpha_w + 3.3\alpha_s\alpha_w \qquad (10)$$

where α_s is the strength of the strongest obstacle and α_w is the strength of the weakest obstacle. The difficulty in applying this mixed approach is that the α_i values for each obstacle type must be known in order to identify the strongest and weakest barriers, which is not the case herein. Thus, we consider linear superposition (Eq. (6)) and root-sum-square superposition (Eq. (8)) as upper and lower limits, respectively, to the irradiation-induced change in yield stress.

4.3.1. Approach I: fitting method

This first approach entails calculating appropriate α_i values that will make the linear sum and root-sum-square system of equations fit the known change in yield stress measured by nanoindentation. Obviously, this approach forces the resulting changes in yield strength to be equal to those measured by nanoindentation. Thus,

the purpose of this approach is to provide a basis for comparison of α values from Approaches II and III.

For linear superposition, Eqs. (2) and (4) are substituted into Eq. (6) for both the proton-irradiated and neutron-irradiated conditions, establishing a system of equations. This system of equations is indeterminate, however, as there are only two equations ($\Delta\sigma_{y,l}^{prot}$ and $\Delta\sigma_{y,l}^{neut}$) with three unknowns ($\alpha_{nc}$, α_v, and α_l). The same approach is applied for root-sum-square superposition in which Eqs. (2) and (4) are substituted into Eq. (8) for both the proton-irradiated and neutron-irradiated conditions, establishing another system of indeterminate equations. But, in studying both the linear and root-sum-square systems of equations, only a finite range exists within which all three α's fall between 0 and 1. These ranges of validity for α_{nc}, α_v, and α_l are provided in Table 6.

4.3.2. Approach II: analytical method, oxides incoherent

In this second approach, α values are calculated directly from analytical expressions, then utilized in the linear sum and root-sum-square superposition expressions to predict irradiation-induced strengthening from microstructure. In this approach, we assume the oxide nanoclusters are incoherent precipitates. Voids and dislocation loops are the other obstacles considered as contributing to strengthening. It is believed that α strengths are dependent upon the size and number density of the obstacle [10,22–24]. Tan and Busby developed size- and density-dependent expressions for α of the obstacles of interest to this study [22]:

$$\text{Incoherent Precipitates } \alpha_{nc}^{incoh} = \frac{0.135}{(1-\nu)^{1/2}\left(1 - 0.816\boldsymbol{d}\sqrt{\boldsymbol{Nd}}\right)}ln\left(\frac{0.816\boldsymbol{d}}{r_0}\right) \qquad (11)$$

$$\text{Voids/Cavities } \alpha_v = \frac{0.383}{(1-v)^{1/2}\left(1-0.816\boldsymbol{d}\sqrt{N\boldsymbol{d}}\right)}ln\left[\frac{0.247\boldsymbol{d}}{r_0}\left(1-0.816\boldsymbol{d}\sqrt{N\boldsymbol{d}}\right)\right] \tag{12}$$

$$\text{Loops (thin plates) } \alpha_l = \frac{0.271\boldsymbol{A}}{(1-v)^{1/2}\sqrt{N\boldsymbol{d}}(16-\pi t\boldsymbol{A})}ln\left(\frac{0.637\boldsymbol{d}}{r_0}\right) \tag{13}$$

where v is Poisson's ratio (~0.33 [24,50–52]), $A = \sqrt{16\pi N d} + 4Nd^2 - \pi^2 Ndt$, and t is the loop thickness (0.165 nm for {111} loops in b.c.c. Fe). The dislocation core radii, r_0, are not well known. But we assume $r_o = b$, and fit the initial calculated values of α_i for each condition to a function $\alpha = k_1 ln(k_2 d)$, following the approach taken in Ref. [22]. Using fitted values for k_2 for the precipitates, voids, and loops, r_0 is ~3.92b, ~0.99b, and ~1.23b for precipitates, voids, and dislocation loops, respectively. Using these expressions from Tan and Busby, and the measured size and number density of obstacles from the present study and ongoing studies by the authors, α values are estimated for each condition (Table 6).

Values of α_v and α_l (voids and loops) determined through Approach II are consistent with those from Approach I + root-sum-square superposition. Conversely, α_{nc} values determined through Approach II are ~3 times greater than those determined through Approach I. The effect of these higher α_{nc} values is compounded when predicting the change in strengthening due to proton or neutron irradiation (−140 MPa and −502 MPa, respectively, using linear superposition, or −405 MPa and −643 MPa, respectively using root-sum-square superposition). These large negative strengthening predictions are inconsistent with measured values, suggesting that the assumption of oxide nanoclusters as incoherent precipitates is not appropriate.

4.3.3. Approach III: fitting/analytical method, oxides coherent

This third approach combines the fitting and analytical methods. For loops and voids, α values are determined from analytical expressions as in Approach II. However, oxide nanoclusters are now assumed to be spherical and coherent. Whereas in Approach II, α_{nc}^{incoh} could be solved directly, the analytical expression for α_{nc}^{coh} depends on three unknown parameters: interfacial energy, γ_{nc} (J/m^2); lattice parameter mismatch between the cluster and matrix, ε; and the shear modulus mismatch between the cluster and the matrix, $\Delta\mu$. So if one attempted to calculate γ_{nc}, ε, and $\Delta\mu$ by fitting the linear sum (Eq. (9)) and root-sum-square (Eq.

(10)) system of equations to the measured change in yield stress, one has more unknowns than equations, resulting in an unsolvable system. Therefore, Approach III evaluates the range of values for which $\Delta\mu$, ε and γ_{nc} are valid by fitting the linear sum and root-sum-square equations to the measured change in yield stress. Fitted γ_{nc} values are averaged across both irradiation particle types to avoid circular logic; average γ_{nc} is used to directly calculate the valid range of α_{nc}^{coh} using either the linear sum or root-sum-square; then finally the irradiation-induced change in yield stress is predicted.

The analytical expression for α_{nc}^{coh}, the strength factor for spherical obstacles that are coherent with the matrix, is given by Ref. [22]:

$$\alpha_{nc}^{coh} = \frac{0.816\gamma_{nc}\boldsymbol{d}}{\mu b^2\left(1-0.816\boldsymbol{d}\sqrt{N\boldsymbol{d}}\right)} + 1.7\left(\frac{\boldsymbol{d}}{b}\right)^{1.5}\varepsilon^{1.5}$$
$$+ 0.0054\left(\frac{\boldsymbol{d}}{b}\right)^{0.275}\left(\frac{\Delta\mu}{\mu}\right)^{1.5} \tag{14}$$

This expression, along with Eqs. (12) and (13), are substituted into linear superposition, Eq. (6) for both the proton- and neutron-irradiated conditions. Because the values for $\Delta\sigma_v^{irr}$, $\Delta\sigma_l^{irr}$, and $\Delta\sigma_{ss}^{irr}$ can be calculated directly, the variables γ_{nc}, ε, and $\Delta\mu$ are the only remaining unknowns for this system of equations, which cannot be solved directly. However, for each case, only a finite range exists within which γ_{nc}, ε, and $\Delta\mu$ are all positive (Fig. 3a). Most importantly, though, solutions for α_{nc}^{coh} for the as-received, proton- and neutron-irradiated conditions fall within narrow bands (Fig. 3b) when considering all possible combinations of γ_{nc}, ε, and $\Delta\mu$, suggesting that as long as reasonable ranges for these parameters are selected, they have little (if any) influence over the predicted yield stress.

A similar fitting followed by direct calculation can also be done for root-sum-square superposition by substituting Eqs. (12–14) into, Eq. (8) for both the proton-irradiated and neutron-irradiated conditions. Similarly, for each case, only a finite range exists within which γ_{nc}, ε, and $\Delta\mu$ are positive (Fig. 3c). Solutions for α_{nc}^{coh} based on all possible combinations of γ_{nc}, ε, and $\Delta\mu$ again fall within a narrow band for each condition (Fig. 3d). Strength factors for nanoclusters calculated by Approach III are summarized in Table 6, and are consistent with values calculated from Approach I, suggesting that the oxides are coherent. The consistency of these

Table 6
Summary of strength factors (α_i) calculated following several modeling and superposition approaches.

	Oxide nanoclusters (α_{nc})			Voids (α_v)		Dislocation loops (α_l)		$\Delta\sigma_y$ (MPa)	
	As-rec'd	Proton	Neutron	Proton	Neutron	Proton	Neutron	Proton	Neutron
Approach I, linear	0.11–0.13			0.03–0.098		0.01–0.12		6	112
Approach I, r-s-s	0.10			0.40–0.85		0.37–0.38		6	112
Approach II, linear	0.37	0.29	0.19	0.65	0.60	0.44	0.44	−140	−502
Approach II, r-s-s								−405	−643
Approach III, linear	0.15–0.16	0.11–0.12	0.07–0.08	0.65	0.60	0.44	0.44	76	−24
Approach III, r-s-s	0.08	0.05–0.06	0.03–0.04					20	96
Measured	–	–	–	–	–	–	–	6	112

values also confirms that the empirical conversion of Eq. (1) is a reasonable estimate. Finally, the individual strengthening contribution from each type of barrier is computed and the overall predicted strengthening is calculated (listed in Table 6 and depicted in Fig. 4). Again, root-sum-square superposition more accurately predicts overall strengthening (20 MPa and 96 MPa for proton and neutron irradiation, respectively) than linear sum (76 MPa and −24 MPa, respectively).

The α strengths vary with oxide nanocluster size using Approach III and root-sum-square superposition, these values are 0.8, 0.05−0.06, and 0.03−0.04, respectively for the as-received, proton-irradiated, and neutron-irradiated conditions. Field et al. [19] reported a similar alpha strength estimate of 0.06 for Cr-rich α' clusters in a model Fe-Cr-Al alloy, while Bergner et al. [20] calculated alpha strengths of 0.03 and 0.134 for α' and NiSiPCr-rich clusters, respectively, using the same dispersed barrier hardening and superposition approaches. The alpha value for dislocation loops in this study, 0.44, is also reasonably consistent with Field's [19] and Bergner's [20] estimates of 0.17−0.33 and 0.44, respectively.

4.4. Critical angle estimate

An alternative method for interpreting the dispersed barrier hardening mechanism is to express strengthening as a function of the critical breakaway angle (ϕ_c). This parameter describes the angle at which a dislocation must climb in order to bypass a barrier. The strengthening equation may be written as [53,54]:

$$\Delta\sigma_y = 1.73\frac{\mu b}{\lambda}\cos\phi_c \qquad (15)$$

where λ is the average interspacing between obstacles ($\lambda = N_{nc}^{-1/3} - d_{nc}$) [54]. A small critical breakaway angle (~0°) indicates that dislocations must climb to bypass the obstacle, whereas larger critical breakaway angles (~90°) suggest that dislocations can shear through the obstacle with little difficulty.

The critical breakaway angle for the oxide nanoclusters is calculated by substituting Eq. (15) into Eq. (6) for the nanoclusters, and using values for α_v and α_l calculated in Approaches II and III above. The resultant critical breakaway angles are 76° and 84° for the proton- and neutron-irradiated specimens, respectively. These angles, nearing 90°, indicate that the oxide nanoclusters are mostly coherent. It is also worth noting that the critical angle is higher for neutron-irradiated than proton-irradiated nanoclusters, suggesting that smaller oxides tend to be more coherent than larger oxides. Observations in the archival literature corroborate this idea: smaller oxides tend to have non-stoichiometric chemistry with Y:Ti
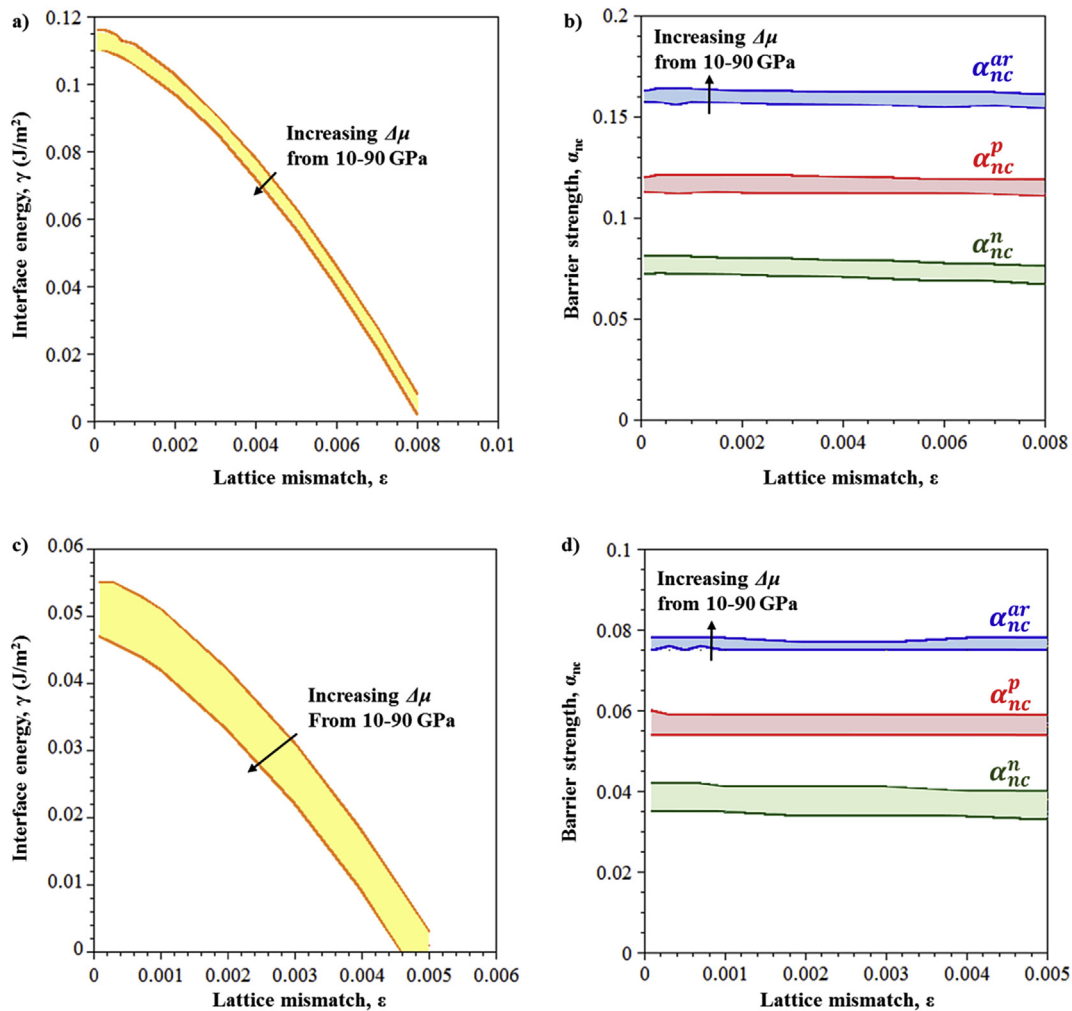

Fig. 3. Solution space for: (a,c) γ_{nc}, ε, and $\Delta\mu$, and (b,d) α_{nc} for as-received (blue), proton-irradiated (red), and neutron-irradiated (green) specimens using Approach III with linear superposition (a,b) and root-sum-square superposition (c,d). (For interpretation of the references to colour in this figure legend, the reader is referred to the web version of this article.)
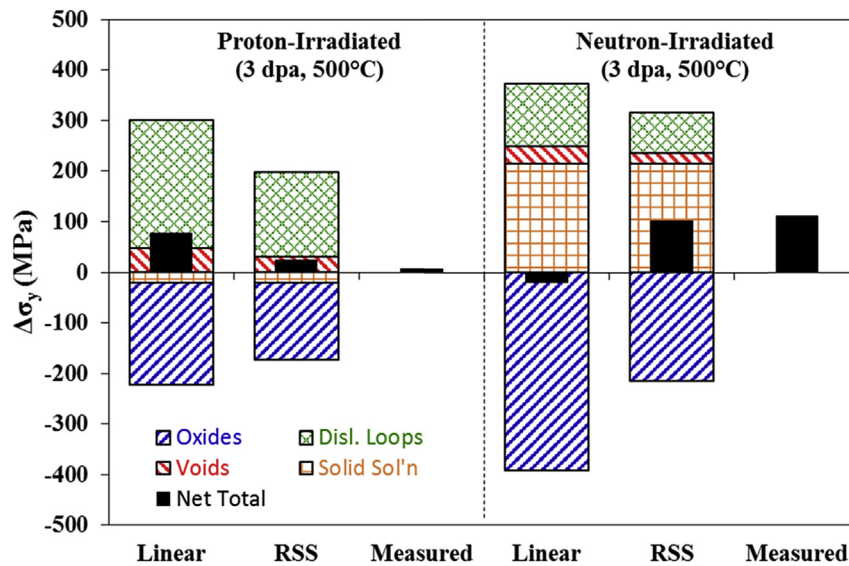
Fig. 4. Calculated effects of dispersed barriers and solid solution strengthening using Approach III with linear or root-sum-square superposition. Solid black bars compare total predicted strengthening to measured strengthening.

ratio ≈ 0.5 [9,13], while larger oxides trend toward a Y:Ti ≈ 1.3 [9,13] with a pyrochlore $Y_2Ti_2O_7$ or orthorhombic Y_2TiO_5 structure [51,55–59].

5. Conclusions

In this study, Fe-9%Cr ODS specimens were irradiated to ~3 dpa at 500 °C using either protons or neutrons. Nanoindentation measured relative changes in hardness as a result of each irradiation condition. Both the dispersed barrier hardening and solid solution strengthening models were applied to relate the microstructure evolution (conducted in a previous study using TEM and APT [27]) to the measured change in macroscopic properties. Based on this experiment, the following conclusions are drawn:

1) The simplified dispersed barrier hardening model alone cannot adequately explain the change in yield stress (measured by nanoindentation) due to proton or neutron irradiation.
2) Irradiation-induced instability of the oxide nanoclusters changes the Ti, Y, and O concentrations in the solid solution matrix. These elemental species contribute to solid solution strengthening; oxygen atoms in particular tend to sit on interstitial sites, and as such, are strong barriers to dislocation motion. Thus, solid solution strengthening is non-negligible in ODS alloys that exhibit oxide dissolution or coarsening under irradiation.
3) A model combining the dispersed barrier hardening and solid solution strengthening mechanisms can reasonably predict irradiation-induced change in yield strength based upon the microstructural and microchemical evolution.
4) The root-sum-square method for superimposing the strengthening effects of dispersed barriers is likely more accurate than linear superposition for irradiated ODS alloys that include a variety of obstacles inhibiting dislocation motion.
5) Small oxide nanoclusters are likely low-strength, coherent obstacles, while larger oxide nanoclusters may tend to be less coherent.

Overall, this work demonstrates that in addition to dispersed barrier hardening, solid solution strengthening must be considered especially for interstitial solutes, in order for the irradiated microstructure in ODS alloys to reasonably predict irradiation-induced hardening.

Acknowledgements

References

[1] S.J. Zinkle, J.T. Busby, Mater. Today 12 (2009) 12.
[2] T. Allen, J. Busby, M. Meyer, D. Petti, Mater. Today 13 (2010) 14.
[3] P. Yvon, F. Carré, J. Nucl. Mater 385 (2009) 217.
[4] L. Barnard, G.R. Odette, I. Szlufarska, D. Morgan, Acta Mater 60 (2012) 935.
[5] A. Certain, S. Kuchibhatla, V. Shutthanandan, D.T. Hoelzer, T.R. Allen, J. Nucl. Mater 434 (2013) 311.
[6] A.G. Certain, K.G. Field, T.R. Allen, M.K. Miller, J. Bentley, J.T. Busby, J. Nucl. Mater 407 (2010) 2.
[7] P. Dubuisson, Y. De Carlan, V. Garat, M. Blat, J. Nucl. Mater 428 (2012) 6.
[8] J. He, F. Wan, K. Sridharan, T.R. Allen, A. Certain, V. Shutthanandan, Y.Q. Wu, J. Nucl. Mater 455 (2014) 41.
[9] J. He, F. Wan, K. Sridharan, T.R. Allen, A. Certain, Y.Q. Wu, J. Nucl. Mater 452 (2014) 87.
[10] C. Hin, B.D. Wirth, J. Nucl. Mater 402 (2010) 30.
[11] R.L. Klueh, D.R. Harries, High-chromium Ferritic and Martensitic Steels for Nuclear Applications, ASTM, 2001.
[12] C. Liu, C. Yu, N. Hashimoto, S. Ohnuki, M. Ando, K. Shiba, S. Jitsukawa, J. Nucl. Mater 417 (2011) 270.
[13] H. Sakasegawa, L. Chaffron, F. Legendre, L. Boulanger, T. Cozzika, M. Brocq, Y. de Carlan, J. Nucl. Mater 384 (2009) 115.
[14] G. Martin, Phys. Rev. 30 (1984) 1424.
[15] R.S. Nelson, J.A. Hudson, D.J. Mazey, J. Nucl. Mater 44 (1972) 318.
[16] K.C. Russell, J. Nucl. Mater 206 (1993) 129.
[17] G.E. Lucas, J. Nucl. Mater 206 (1993) 287.
[18] G.S. Was, Fundamentals of Radiation Materials Science: Metals and Alloys, Springer, 2007, pp. 600–610.
[19] K.G. Field, X. Hu, K.C. Littrell, Y. Yamamoto, L.L. Snead, J. Nucl. Mater 465 (2015) 746.

[20] F. Bergner, C. Pareige, M. Hernández-Mayoral, L. Malerba, C. Heintze, J. Nucl. Mater 448 (2014) 96.
[21] S.I. Porollo, A.M. Dvoriashin, A.N. Vorobyev, Y.V. Konobeev, J. Nucl. Mater 256 (1998) 1.
[22] L. Tan, J.T. Busby, J. Nucl. Mater 465 (2015) 724.
[23] S. Kotrechko, V. Dubinko, N. Stetsenko, D. Terentyev, X. He, M. Sorokin, J. Nucl. Mater 464 (2015) 6.
[24] M.J. Alinger, On the Formation and Stability of Nanometer Scale Precipitates in Ferritic Alloys during Processing and High Temperature Service, 2004.
[25] S. Ohtsuka, S. Ukai, M. Fujiwara, T. Kaito, T. Narita, Mater. Trans. 46 (2005) 487.
[26] J.F. Ziegler, J.P. Biersack, SRIM — The Stopping and Range of Ions in Matter, 2008.
[27] M.J. Swenson, J.P. Wharry, J. Nucl. Mater 467 (2015) 97.
[28] J.M. Hyde, E.A. Marquis, K.B. Wilford, T.J. Williams, Ultramicroscopy 111 (2011) 440.
[29] P. Hosemann, D. Kiener, Y. Wang, S.A. Maloy, J. Nucl. Mater 425 (2012) 136.
[30] D. Kramer, H. Huang, M. Kriese, J. Robach, J. Nelson, A. Wright, Acta Mater 47 (1999) 333.
[31] S.S. Chiang, J. Appl. Phys. 53 (1982) 298.
[32] M. Yoshioka, J. Appl. Phys. 76 (1994) 7790.
[33] C.K. Dolph, Plastic Deformation and Effective Strain Hardening Coefficient of Irradiated Fe-9wt%Cr ODS Alloy by Nanoindentation and TEM, Boise State University, 2015.
[34] Z. Huang, A. Harris, S.A. Maloy, P. Hosemann, J. Nucl. Mater 451 (2014) 162.
[35] B. Yao, D.J. Edwards, R.J. Kurtz, J. Nucl. Mater 434 (2013) 402.
[36] C.M. Parish, K.G. Field, A.G. Certain, J.P. Wharry, J. Mater. Res. 30 (2015) 1275.
[37] P. Hosemann, E. Stergar, L. Peng, Y. Dai, S.A. Maloy, M.A. Pouchon, K. Shiba, D. Hamaguchi, H. Leitner, J. Nucl. Mater 417 (2011) 274.
[38] J.T. Busby, M.C. Hash, G.S. Was, J. Nucl. Mater 336 (2005) 267.
[39] A.C. Fischer-Cripps, Nanoindentation, Springer, New York, 2011.
[40] D.A. McClintock, M.A. Sokolov, D.T. Hoelzer, R.K. Nanstad, J. Nucl. Mater 392 (2009) 353.
[41] A. Ramar, N. Baluc, R. Schäublin, J. Nucl. Mater 367—370 (2007) 217.
[42] A. Seeger, J. Diehl, S. Mader, H. Rebstock, Philos. Mag. 2 (1957) 323.
[43] I. Kubena, B. Fournier, T. Kruml, J. Nucl. Mater 424 (2012) 101.
[44] G.R. Odette, G.E. Lucas, Radiat. Eff. Defects Solids 144 (1998) 189.
[45] J.W. Martin, Micromechanisms in Particle-hardened Alloys, 1980.
[46] Q. Lu, W. Xu, S. Van Der Zwaag, Comput. Mater. Sci. 84 (2014) 198.
[47] F.B. Pickering, Physical Metallurgy and the Design of Steels, Applied Science Publishers LTD, London, 1978.
[48] W.C. Leslie, Metall. Trans. 3 (1972) 5.
[49] R.W. Cahn, P. Haasen, Physically Metallurgy, fourth ed., III, Amsterdam, 1996, pp. 2034—2035.
[50] J. Malaplate, F. Mompiou, J.-L. Béchade, T. Van Den Berghe, M. Ratti, J. Nucl. Mater 417 (2011) 205.
[51] S. Ukai, T. Okuda, M. Fujiwara, T. Kobayashi, S. Mizuta, H. Nakashima, J. Nucl. Sci. Technol. 39 (2002) 872.
[52] T. Tanno, S. Ohtsuka, Y. Yano, T. Kaito, Y. Oba, M. Ohnuma, S. Koyama, K. Tanaka, J. Nucl. Mater 440 (2013) 568.
[53] R. Abbaschian, L. Abbaschian, R.E. Reed-Hill, Physical Metallurgy Principles, Fourth, Cengage Learning, Stamford, CT, 2010.
[54] A. Xu, C. Beck, D.E.J. Armstrong, K. Rajan, G.D.W. Smith, P.A.J. Bagot, S.G. Roberts, Acta Mater 87 (2015) 121.
[55] H. Kishimoto, R. Kasada, O. Hashitomi, A. Kimura, J. Nucl. Mater 386—388 (2009) 533.
[56] Y. Wu, E.M. Haney, N.J. Cunningham, G.R. Odette, Acta Mater 60 (2012) 3456.
[57] S. Yamashita, N. Akasaka, S. Ohnuki, J. Nucl. Mater 329—333 (2004) 377.
[58] S.Y. Zhong, J. Ribis, V. Klosek, Y. de Carlan, N. Lochet, V. Ji, M.H. Mathon, J. Nucl. Mater 428 (2012) 154.
[59] M. Klimiankou, R. Lindau, A. Möslang, J. Nucl. Mater 329—333 (2004) 347.